

Properties of magnetic shape memory alloys in martensitic phase

Chhayabrita Maji*

Department of Materials Science, Indian Association for the Cultivation of Science, 2A and 2B Raja S.C. Mullick Road, Jadavpur, Kolkata 700 032, India

The Heusler alloys that exhibit reversible martensitic transition show multifunctional properties including magnetic shape memory effect. The properties of two kinds of magnetic shape memory alloys are studied, where magnetic field-induced strain is driven by two different mechanisms. The properties differ in martensitic phase with composition and thus they are studied in martensitic phase. The crystal structure (X-ray diffraction), magnetic behaviour (SQUID), transport analysis (four-probe method), magneto-transport trend (up to 8 T), magnetocaloric effect (around room-temperature), electronic structure (X-ray photoelectron spectroscopy and *ab initio* calculation), surface characterization (ultraviolet photoelectron spectroscopy and inverse photoelectron spectroscopy) are discussed for the martensitic phase. Analysis of the properties reveals alloys with possible applicability at room temperature with low magnetic field.

Keywords: Magnetoresistance, martensitic transition, shape memory alloys.

THE shape memory alloys (SMAs) have emerged as smart advanced materials in the recent past due to wide applications in bioengineering^{1–8}, aerospace^{1,9–11}, robotics^{12–14}, consumer products and industrial applications^{15–17}, structures and composites¹⁸, automotive industry^{19–21}, actuators and micro-electromechanical systems (MEMS)^{1,2,22–24}, and in fashion²⁵. The SMAs are capable of memorizing their original shape. They return to their original shape after removal of thermal and mechanical procedures. This is known as shape memory effect. The shape change is accompanied by structural changes. The structural change exists in two different phases – the high-temperature phase (austenite) and low temperature phase (martensite). The phase change is reversible and could be driven by temperature and mechanical load. Apart from temperature and load, the reversible phase transition is also triggered by magnetic field. Such SMAs are known as magnetic shape memory alloys (MSMAs).

The MSMAs consists of ternary, magnetic, intermetallic Heusler alloys defined by the generic formula X_2YZ with $X = \text{Ni, Co, Cu, Pd, etc.}$ $Y = \text{Mn, Ti, Hf, Zr, etc.}$ and

$Z = \text{Ga, Al, Sn, In, Sb, etc.}$ The MSMA austenite phase crystallizes in ordered $L2_1$ structure that can be considered as four interpenetrating f.c.c. sublattices with atoms at $(0, 0, 0)$, $(1/4, 1/4, 1/4)$, $(1/2, 1/2, 1/2)$, $(3/4, 3/4, 3/4)$ locations respectively (Figure 1). When the temperature is decreased, they undergo martensitic transformation and acquire a number of structures. The martensitic phase could be weakly modulated with tetragonal or orthorhombic or monoclinic crystal structure. The martensitic transition (MT) is a first-order structural transformation. Due to first-order phase transformation, it shows hysteresis during heating and cooling. The characteristic transformation temperatures are called austenitic start (A_S), austenitic finish (A_F) (during heating), and martensitic start (M_S), martensitic finish (M_F) (during cooling) (Figure 2).

The Heusler alloys are traditionally considered to be local moment systems^{26,27}. The Mn-based ($X_2\text{MnZ}$) alloys are the most studied system in Heusler alloys. The magnetic moment is mainly localized on Mn. The localized character of the magnetization results from the exclusion of minority spin electrons from the Mn 3d states. The magnetism arises due to the RKKY-type indirect exchange interaction. When the interaction is mediated by the X conduction electrons, the alloy is ferromagnetic and if it is mediated by the Z conduction electrons, it can have either sign depending on the position of the Fermi level (E_F) in the Mn– Z p - d hybrid states.

The shape memory effect originates from magnetic field-induced strain (MFIS). There are different classes of materials in the Heusler alloy system, where MFIS is governed by two different mechanisms: (i) martensite variant reorientation as a result of magnetic field-induced twin boundary motion, and (ii) magnetic field-induced reverse phase transformation²⁸. In the former mechanism, if the magnetocrystalline anisotropy energy (MAE) of a magnetic field-favoured martensite variant is larger than the energy required for twin boundary motion, then that variant will grow at the expense of others, resulting in a field-induced macroscopic shape change. Few examples are Ni–Mn–Ga, Ni–Co–Al, Ni–Fe–Ga, Ni–Co–Ga, etc.²⁹. The MAE is limited by the saturation magnetic field, above which it does not increase with the field. So actuation stress level is also limited by the field. The MAE is also crystal orientation-dependent. The field-induced variant reorientation mechanism is limited to single

*e-mail: chhayabrita@gmail.com

crystals. Thus, the high cost of single crystals and low actuation stress levels restrict the potential applications of these MSMAs.

The second mechanism for MFIS involves the Zeeman energy (ZE) difference between the parent and martensitic phase. The ZE is crystal orientation-independent. In this case, MAE of the martensitic phase is very less or negligible. The ZE difference is not saturated with the field. So large actuation stress level (up to 200 MPa) with the MFIS is obtained in the polycrystals²⁸. The MFIS could be maximized by maximizing the ZE difference. The ZE difference is maximized by increasing the difference between the saturation magnetization of both phases. When a ferromagnetic phase transforms to a paramagnetic or antiferromagnetic phase, or vice-versa, the ZE difference is increased. Off-stoichiometric Ni–Mn–Sn,

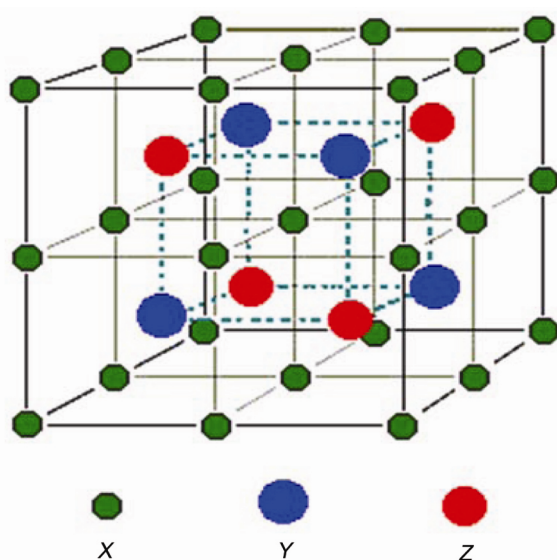


Figure 1. The L₂₁ crystal structure of Heusler alloys (figure reproduced from <http://www.nims.go.jp/mmu/tutorials/halfmetal.html>).

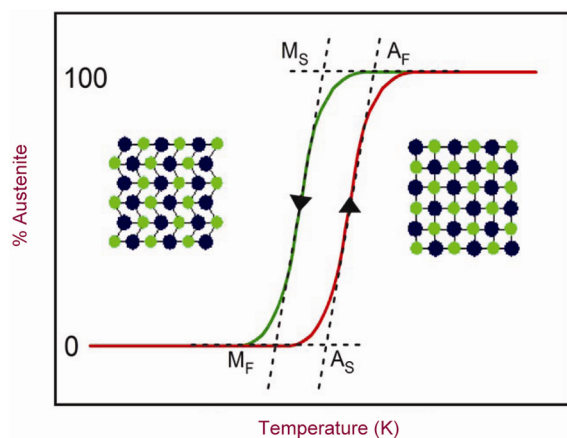


Figure 2. Schematic of martensitic transformation (figure reproduced from <http://memry.com/nitinol-iq/nitinol-fundamentals/transformation-temperatures>).

Ni–Mn–In, Ni–Mn–Sb and Ni–Co–Mn–In are the promising materials for this mechanism, in which ferromagnetic austenite transforms to the non-magnetic (para or anti-ferro) martensitic phase²⁸.

In austenitic phase the behaviour of both kinds of MSMAs is similar. They crystallize into L₂₁ cubic structure^{30–32}. The austenitic phase is predominantly ferromagnetic^{30,31,33}. The transport behaviour is metallic^{30,34,35}. The negative magnetoresistance (MR) is obtained with similar values (around 5%)^{30–33}. The magnetocaloric effect is not obtained in the austenitic phase. Further, the electronic structure is also similar in the austenitic phase^{36–38}. In this article the properties of both kinds of MSMAs are studied in the martensitic phase. The properties of the martensitic phase are highly composition-dependent. For the first kind of MSMA, Ni_{2+x}Mn_{1-x}Ga polycrystals are studied. For the second kind of MSMA, Ni₂Mn_{1+x}Sn_{1-x}, Ni₂Mn_{1+x}In_{1-x}, Ni_{1.8}Co_{0.2}Mn_{1+x}In_{1-x} polycrystalline Heusler alloys are studied. The crystal structure, magnetic behaviour, transport analysis, magneto-transport trend, magnetocaloric effect (MCE) and electronic structure are discussed for the martensitic phase.

Experimental and theoretical methods

The polycrystalline ingots of Heusler alloys are prepared by arc-melting appropriate amount of high purity ($\geq 99.99\%$) constituent elements under argon atmosphere, which are annealed at various temperatures (composition-dependent) with subsequent quenching to ice water^{30,31,33}. The actual composition is obtained by averaging the energy-dispersive X-ray analysis from different parts of the alloy. The actual composition is within 1% of the intended composition. The homogeneity in different parts of the sample is within 3%. The structural and magnetic transition temperatures are determined by differential scanning calorimetry (DSC). The values of the transition temperatures are tabulated for Ni_{2+x}Mn_{1-x}Ga (Table 1)³⁰, Ni₂Mn_{1+x}In_{1-x} (Table 2)³⁵ and Ni–Co–Mn–In (Table 3)³⁹. Figure 3 shows the phase diagram for characteristic transition temperatures of Ni₂Mn_{1+x}Sn_{1-x}.

The room-temperature X-ray diffraction (XRD) is done using CuK α radiation. The Rietveld refinement and LeBail fitting are performed to determine the crystal structure and lattice parameter. The zero-field-cooled (ZFC) and field-cooled (FC) thermomagnetization at 0.05 T was measured in the temperature range $5 \leq T \leq 300$ K using superconducting quantum interference device from Quantum Design. The MR measurements were carried out by standard four-probe technique using a home-made resistivity set-up with superconducting magnet system (Oxford Instruments Inc., UK). The magnetic field (maximum $\mu_0 H = 8$ T) was applied parallel to current flow direction. The photoemission spectra were recorded using monochromatic AlK α (1486.6 eV)

radiation (for $\text{Ni}_2\text{Mn}_{1+x}\text{Sn}_{1-x}$) and non-monochromatic $\text{MnK}\alpha$ (for $\text{Ni}_{2+x}\text{Mn}_{1-x}\text{Ga}$) at an operating pressure of 1×10^{-10} mbar. The electron detection was carried out using Gammadata Scienta analyzer R4000 (for $\text{Ni}_2\text{Mn}_{1+x}\text{Sn}_{1-x}$) and an electron energy analyser of Specs GmbH (for $\text{Ni}_{2+x}\text{Mn}_{1-x}\text{Ga}$). The energy resolution was 0.44 eV and 1 eV respectively. The ultraviolet photoelectron spectroscopy (UPS) is performed using He I radiation. The energy resolution is 120 meV. Inverse photoelectron spectroscopy (IPES) in the isochromat mode was performed using an electron source (Stoffel Johnson) and a CaF/acetone photon detector. The total energy resolution was about 0.5 eV.

The *ab initio* relativistic spin-polarized FPLAPW calculations were performed using the WIEN97 code with the generalized gradient approximation for exchange correlation for $\text{Ni}_{2+x}\text{Mn}_{1-x}\text{Ga}$ (ref. 36). The *ab initio* electronic structure calculations for $\text{Ni}_2\text{Mn}_{1+x}\text{Sn}_{1-x}$ were carried out using the PAW method as implemented in the VASP code within GGA for the exchange correlation functional⁴⁰. A supercell consisting of $5 \times 5 \times 1$ primitive cells of the $L2_1$ crystal structure was considered to calculate the behaviour of excess Mn substitution at Sn sites⁴¹. The IPES spectra were calculated using the Korringa-Kohn-Rostoker method³⁸.

Martensitic crystal structure

The martensitic phase crystal structure depends on the composition. The martensitic crystal structure is tetragonal with Fmmm space group for $\text{Ni}_{2+x}\text{Mn}_{1-x}\text{Ga}$ (Figure 4; $a = b = 5.469 \text{ \AA}$ and $c = 6.517 \text{ \AA}$). $\text{Ni}_{1.8}\text{Co}_{0.2}\text{Mn}_{1+x}\text{In}_{1-x}$

Table 1. Characteristic transition temperatures of $\text{Ni}_{2+x}\text{Mn}_{1-x}\text{Ga}$ found using DSC

Composition	M_s (K)	M_f (K)	A_s (K)	A_f (K)
Ni_2MnGa	207	182	212	223
$\text{Ni}_{2.2}\text{Mn}_{0.8}\text{Ga}$	350	329	360	378

Table 2. Structural and magnetic transition temperatures of $\text{Ni}_2\text{Mn}_{1+x}\text{In}_{1-x}$ obtained from DSC

x	M_s (K)	M_f (K)	A_s (K)	A_f (K)	T_c^a (K)
0.32					312
0.36	258	201	215	266	314
0.42	391	369	374	394	
0.48	457	437	444	466	

Table 3. Structural and magnetic transition temperatures of Ni-Co-Mn-In obtained from DSC

Sample	M_s (K)	M_f (K)	A_s (K)	A_f (K)	T_c^a (K)
NCMI1	346	317	329	359	390
NCMI2	335	292	312	349	397

has a similar tetragonal martensitic crystal structure (space group Fmmm) as shown in Figure 5 for $\text{Ni}_{1.8}\text{Co}_{0.2}\text{Mn}_{1.47}\text{In}_{0.53}$ ($a = b = 5.59 \text{ \AA}$, $c = 6.8 \text{ \AA}$). Whereas the $\text{Ni}_2\text{Mn}_{1+x}\text{In}_{1-x}$ composition without Co doping undergoes structural change to monoclinic structure (10 M

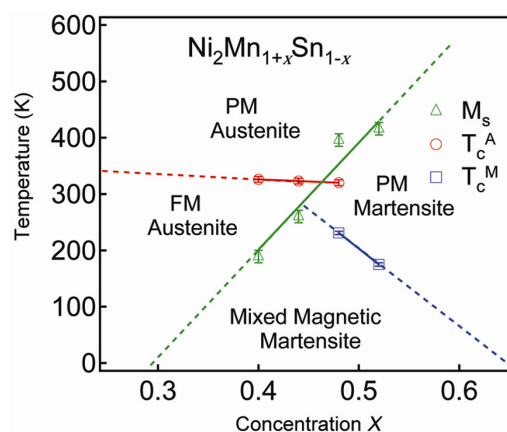


Figure 3. Phase diagram of $\text{Ni}_2\text{Mn}_{1+x}\text{Sn}_{1-x}$ alloys obtained from DSC, magnetization and resistivity measurements.

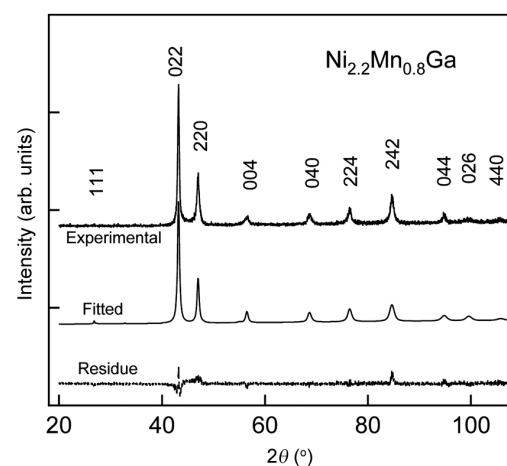


Figure 4. Room temperature XRD pattern of $\text{Ni}_{2+x}\text{Mn}_{1-x}\text{Ga}$ with Rietveld fitting and residue. The martensitic phase has single-phase tetragonal structure³⁰.

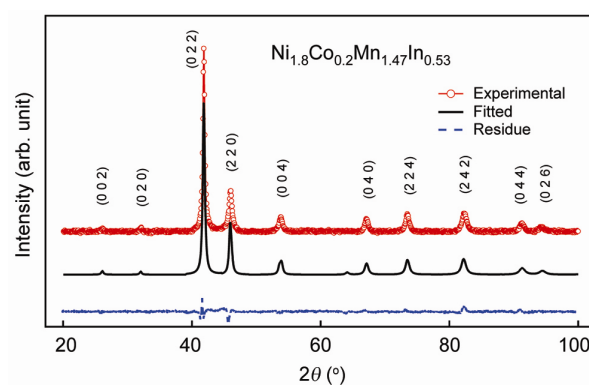


Figure 5. Martensitic-phase tetragonal crystal structure of $\text{Ni}_{1.8}\text{Co}_{0.2}\text{Mn}_{1.47}\text{In}_{0.53}$ with fitting and residue³⁹.

modulated with space group P2/m). Figure 6 b shows the monoclinic structure with $\beta = 89.06^\circ$, $a = 4.42 \text{ \AA}$, $b = 5.54 \text{ \AA}$ and $c = 22.05 \text{ \AA}$. The replacement of In by Sn, i.e. $\text{Ni}_2\text{Mn}_{1+x}\text{Sn}_{1-x}$, results in orthorhombic structure in the martensitic phase with Pmma space group. Interestingly, the orthorhombic structure consists of two phases, namely 14-layered (14L) and four-layered (4L). Figure 6 a shows the combined fitted 4L and 14L orthorhombic

phases for $\text{Ni}_2\text{Mn}_{1.48}\text{Sn}_{0.52}$ (14L: $a = 4.26 \text{ \AA}$, $b = 28.86 \text{ \AA}$, $c = 5.54 \text{ \AA}$ and 4L: $a = 4.32 \text{ \AA}$, $b = 5.78 \text{ \AA}$, $c = 8.70 \text{ \AA}$).

The *ab initio* calculation⁴⁰ for $\text{Ni}_2\text{Mn}_{1+x}\text{Sn}_{1-x}$ shows that with increase in Mn2 concentration, the Ni atoms move towards both Mn1 and Mn2. The resultant movement is along a lattice parameter. The movement of the Ni atoms is away from the Sn atoms. The Ni atoms moving away from the Sn atoms results in reduced repulsion felt by the electrons on Ni from lone pair on Sn. Hence the energy of the system is lowered and structural transition occurs for $\text{Ni}_2\text{Mn}_{1+x}\text{Sn}_{1-x}$. The lone pair electrons is also present in In. So, the mechanism proposed should be valid for the In system as well. However, the bond length between Ni–In, Ni–Sn and Co–In would be different which may give rise to different crystal structure of the martensitic phase.

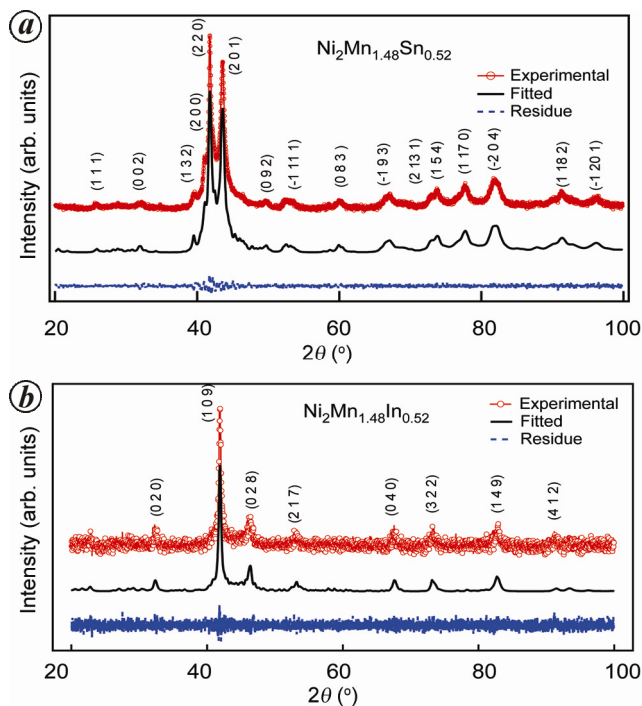


Figure 6. Room temperature XRD pattern with fitting and residue of (a) $\text{Ni}_2\text{Mn}_{1+x}\text{Sn}_{1-x}$ and (b) $\text{Ni}_2\text{Mn}_{1+x}\text{In}_{1-x}$.

Magnetic behaviour

The martensitic phase of $\text{Ni}_{2+x}\text{Mn}_{1-x}\text{Ga}$ has a ferromagnetic ground state³⁰. Figure 7 shows the thermomagnetization behaviour of Ni_2MnGa . The sudden decrease in the magnetization upon martensitic transition reveals that although the ground state is ferromagnetic, the magnetic moment of the martensitic phase is less than the austenite phase. The temperature hysteresis is clearly observable at the first-order martensitic transition. A small dip is observed around the pre-martensitic transition, which occurs due to phonon softening. Unlike $\text{Ni}_{2+x}\text{Mn}_{1-x}\text{Ga}$, $\text{Ni}_2\text{Mn}_{1+x}\text{In}_{1-x}$, $\text{Ni}_{1.8}\text{Co}_{0.2}\text{Mn}_{1+x}\text{In}_{1-x}$ and $\text{Ni}_2\text{Mn}_{1+x}\text{Sn}_{1-x}$ have mixed magnetic (ferro and antiferro) ground state^{31,33}. The antiferromagnetic coupling occurs between Mn at Mn site (Mn1) and Mn at Sn (In) site (Mn2)⁴¹. Figure 8 shows a typical magnetization behaviour of $\text{Ni}_2\text{Mn}_{1+x}\text{In}_{1-x}$. The splitting between ZFC and FC below the structural transition temperatures M_F and A_S indicates the presence of magnetically inhomogeneous phase and competition between them. The blocking of the martensitic phase is observed at 14 T magnetic field. The

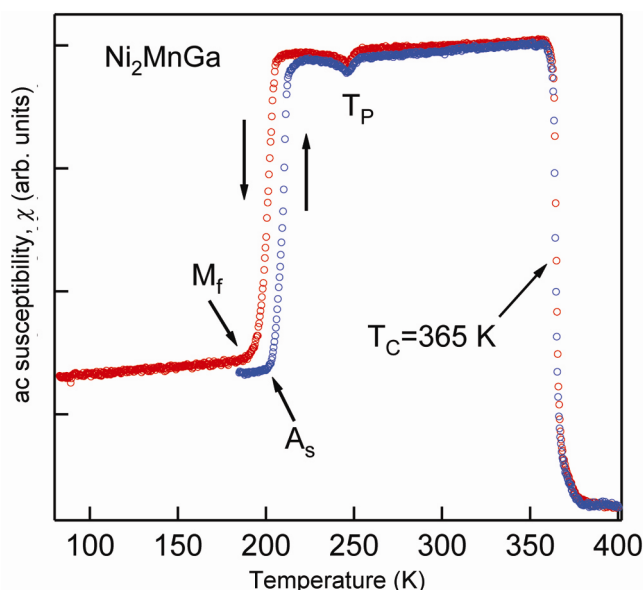


Figure 7. Magnetization behaviour of Ni_2MnGa (ref. 30).

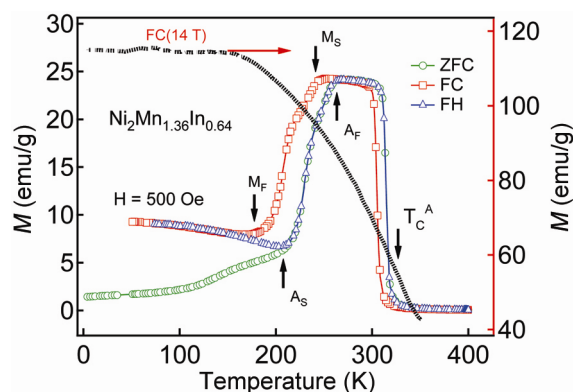


Figure 8. Magnetization behaviour of $\text{Ni}_2\text{Mn}_{1.36}\text{In}_{0.64}$ (ref. 33).

Co doping in Ni–Mn–In alloys further increases the magnetic moment and the martensitic transition occurs above room temperature (Figure 9). The huge change in the magnetization at the martensitic transition with the applied magnetic field in Ni–Co–Mn–In alloys gives the large inverse MCE (ref. 39).

The Ni–Mn–Sn alloys have less magnetic moment (Figure 10) compared to Ni–Mn–In alloys in the austenitic phase. In the austenitic phase of Ni–Mn–In alloys Mn1 and Mn2 atoms have ferromagnetic coupling, while in the Ni–Mn–Sn alloys Mn1 and Mn2 atoms have weak antiferromagnetic coupling. This difference might be related with the larger atomic size of In than Sn, and higher lattice parameter of Ni–Mn–In alloys compared to Ni–Mn–Sn alloys. A weak antiferromagnetic coupling ($J_{ij} = -10$ meV) between Mn1 and Mn2 is present in the austenitic phase of $\text{Ni}_2\text{Mn}_{1+x}\text{Sn}_{1-x}$ (ref. 42). The antiferromagnetic exchange interaction is enhanced by a decrease in the Mn1–Mn2 distance upon the martensitic transition due to change in the lattice parameter. The antiferromagnetic exchange ($J_{ij} = -30$ meV) between Mn1

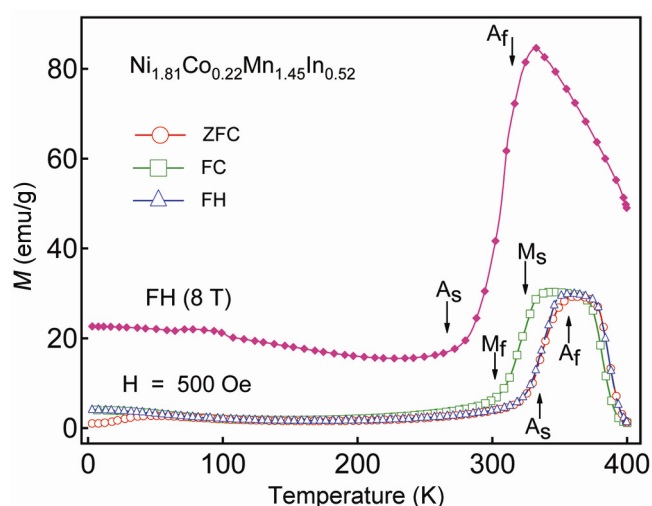


Figure 9. Magnetization behaviour of $\text{Ni}_{1.81}\text{Co}_{0.22}\text{Mn}_{1.45}\text{In}_{0.52}$.

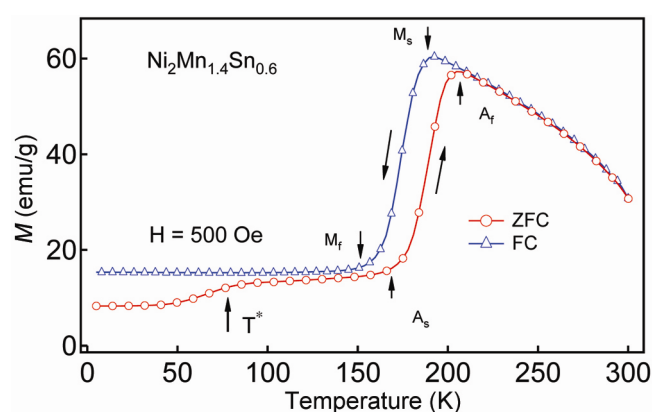


Figure 10. Magnetization behaviour of $\text{Ni}_2\text{Mn}_{1.4}\text{Sn}_{0.6}$ (ref. 31).

and Mn2 is enhanced in the martensitic phase⁴². Thus the magnetic ground state in the martensitic phase has both ferromagnetic (Mn1–Mn1) and antiferromagnetic (Mn1–Mn2) spin alignment. The step-like anomaly in ZFC (marked as T^*) is due to the drop in magnetization arising from the competition between ferromagnetic and antiferromagnetic interaction. The exchange bias phenomenon is reported below T^* temperature^{43,44}. The competing magnetic interactions lead to spin freezing and re-entrant spin glass-like behaviour at the low-temperature martensitic phase⁴³.

Figure 11a shows the isothermal magnetization at 80 K for $0.40 \leq x \leq 0.52$. It clearly reveals that the saturation magnetization decreases with increasing Mn2 (x) concentration. Figure 11b shows the total magnetic moment per formula unit (μ_m) and the coercivity of $\text{Ni}_2\text{Mn}_{1+x}\text{Sn}_{1-x}$ at 80 K as a function of x . The magnetic moment linearly decreases with increasing x , while

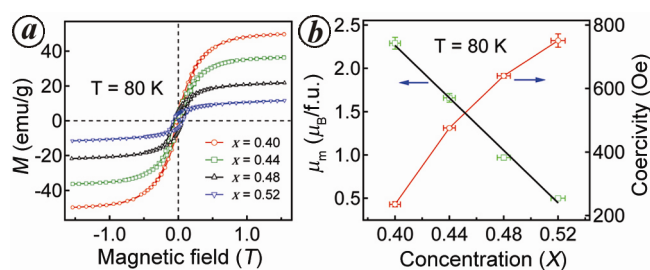


Figure 11. *a*, Isothermal magnetization curve at 80 K for $\text{Ni}_2\text{Mn}_{1+x}\text{Sn}_{1-x}$. *b*, Magnetic moment per formula unit (μ_m) and coercivity of $\text{Ni}_2\text{Mn}_{1+x}\text{Sn}_{1-x}$ at 80 K as a function of x .

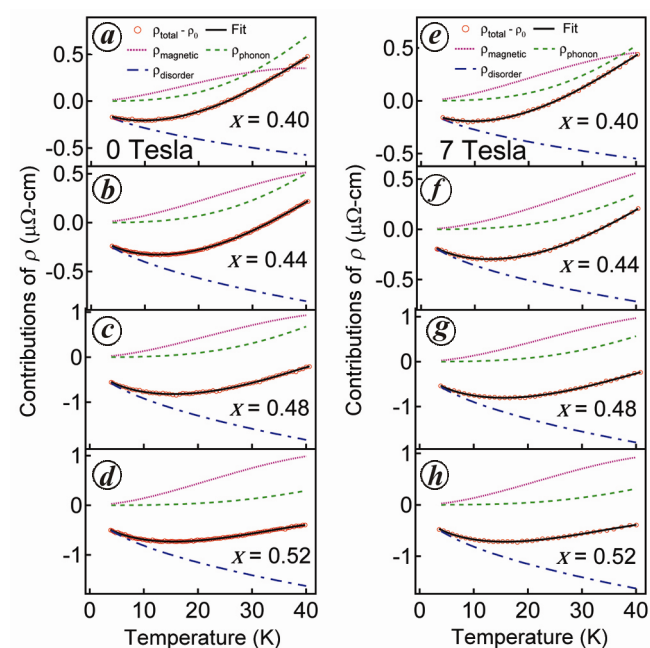


Figure 12. Different contributions to resistivity (ρ_{phonon} , ρ_{magnetic} and ρ_{disorder}) deduced by fitting the experimental data with eq. (1) for $\text{Ni}_2\text{Mn}_{1+x}\text{Sn}_{1-x}$ under (*a–d*) ZFC (0 T) and (*e–h*) FC (7 T)³⁴.

Table 4. The parameters obtained for $\text{Ni}_2\text{Mn}_{1+x}\text{Sn}_{1-x}$ from least square fitting of ZFC resistivity behaviour by eq. (1)³⁴

x	ρ_0 ($\mu\Omega\text{-cm}$)	A ($\mu\Omega\text{-cm}$)	$B \times 10^{-4}$ ($\mu\Omega\text{-cm}/\text{K}^2$)	$C \times 10^{-5}$ ($\mu\Omega\text{-cm}/\text{K}^{5/2}$)	θ_D (K)	$D \times 10^{-2}$ ($\mu\Omega\text{-cm}/\text{K}^{1/2}$)
0.40	137	26.44 ± 1.28	11.6 ± 0.7	14.9 ± 3.2	251 ± 4	9.1 ± 0.5
0.44	155	19.62 ± 0.79	11.1 ± 0.3	12.4 ± 0.4	253 ± 4	12.7 ± 0.2
0.48	256	28.53 ± 3.11	21.3 ± 1.1	24.5 ± 1.4	260 ± 10	29.0 ± 0.9
0.52	251	15.57 ± 2.98	23.7 ± 0.7	25.6 ± 0.9	284 ± 19	26.5 ± 0.5

Table 5. The parameters obtained for $\text{Ni}_2\text{Mn}_{1+x}\text{Sn}_{1-x}$ from least square fitting of FC resistivity behaviour by eq. (1)³⁴

x	ρ_0 ($\mu\Omega\text{-cm}$)	A ($\mu\Omega\text{-cm}$)	$B \times 10^{-4}$ ($\mu\Omega\text{-cm}/\text{K}^2$)	$C \times 10^{-5}$ ($\mu\Omega\text{-cm}/\text{K}^{5/2}$)	θ_D (K)	$D \times 10^{-2}$ ($\mu\Omega\text{-cm}/\text{K}^{1/2}$)
0.40	136	20.4 ± 0.4	11.4 ± 1.2	13.5 ± 1.2	253 ± 2	8.6 ± 0.4
0.44	153	13.7 ± 0.2	8.9 ± 0.7	8.7 ± 1.2	253 ± 2	11.3 ± 0.2
0.48	253	23.8 ± 0.5	20.8 ± 1.7	23.3 ± 1.2	260 ± 3	28.4 ± 0.8
0.52	248	16.5 ± 0.1	21.0 ± 0.5	24.0 ± 1.2	283 ± 2	25.7 ± 0.5

coercivity increases with increasing x . At 80 K all the compositions are in martensitic phase; thus a decrease in the magnetic moment with increasing x confirms the presence of strong antiferromagnetic coupling between Mn1 and Mn2 atoms in the martensitic phase. The coercivity in the martensitic phase might be due to spin pinning or domain wall pinning caused by the antiferromagnetic spins. As the antiferromagnetic spins increase with increasing Mn2 (x), pinning also increases, which results in increase of coercivity⁴⁵.

Transport analysis

The electrical resistivity in ideal Heusler alloys (X_2YZ) arises from two main sources, scattering of electrons by lattice vibrations and scattering from the interaction with the spin system⁴⁶. The transport property of Ni_2MnGa is dominated by electron–magnon and electron–phonon scattering⁴⁷. The resistivity behaviour of $\text{Ni}_{2+x}\text{Mn}_{1-x}\text{Ga}$ is metallic with sudden increase in resistivity at the martensitic transition (see Biswas *et al.*³⁰, figure 1 *a*).

The very basic property of electrical resistivity in metals is modified by the presence of disorder in the crystal-line system. In the off-stoichiometric Heusler alloys, martensitic transformation and disorder effects (site and magnetic) significantly modify the electrical resistivity^{48,49}. The martensitic transition enhances the structural and magnetic disorder in the system. Unlike $\text{Ni}_{2+x}\text{Mn}_{1-x}\text{Ga}$, the second kind of Heusler alloys exhibits low temperature anomaly as shown in Figure 12 for $\text{Ni}_2\text{Mn}_{1+x}\text{Sn}_{1-x}$. The contribution from different scattering mechanisms which are responsible for anomalous resistivity behaviour at low temperature in the martensitic phase has been estimated through experimental data fitting by eq. (1).

$$\rho_{\text{total}}(T) = \rho_0 + A \left(\frac{T}{\theta_D} \right)^3 \int_0^{\theta_D/T} \frac{x^3}{(e^x - 1)(1 - e^{-x})} dx + (BT^2 - CT^{5/2}) - D\sqrt{T}, \quad (1)$$

where ρ_0 is the residual resistivity due to scattering of electrons by defects and impurities that are temperature-independent, A the measure of electron scattering by phonons, B and C the measure of diffusive spin excitation, and D represents the localized states and electron–electron interaction. From the least square fitting by eq. (1), the individual contributions to the total resistivity are plotted (Figure 12). Tables 4 (ZFC) and 5 (FC) summarizes the fitting coefficients.

The magnetic disorder scattering contribution is maximum and increases with Mn2 concentration. The $BT^2 - CT^{5/2}$ variation in Tables 4 and 5 confirms the spin-freezing state in the martensitic phase where impurity spins (Mn2) are short-range antiferromagnetically coupled to Mn1. The scattering of electrons by phonons is influenced by coexistence of two martensitic structural phases. The Debye temperature (θ_D in Tables 4 and 5) for $x = 0.40\text{--}0.48$ increases with increasing Mn2 concentration. The resistivity behaviour with applied magnetic field implies strong interplay of structural and magnetic states in the martensite phase. The electron–electron interaction with localized states also exists. The $-\sqrt{T}$ variation of the low-temperature resistivity anomaly predicts the coexistence of extended and localized states. Further, the application of magnetic field reduces the phase coherence resulting in decrease in the magnitude of D in the FC condition.

Similar to Ni–Mn–Sn alloys, the Ni–Mn–In alloys display resistivity minima at low temperature as shown in

Figure 13 *a* and *b* for 0 and 7 T respectively. Unlike $\text{Ni}_2\text{Mn}_{1+x}\text{Sn}_{1-x}$, under 7 T magnetic field, resistivity upturn disappears for the composition $x = 0.36$ and resistivity behaviour is almost similar to the composition $x = 0.32$. This is due to the fact that under 7 T magnetic field at 5 K, only a small fraction (10%) of the martensitic phase is present. The presence of large austenitic phase fraction (90%) enhances the structural and magnetic order. The disappearance of resistivity minima with magnetic field is not observed for Co-doped $\text{Ni}_2\text{Mn}_{1+x}\text{In}_{1-x}$ (Figure 14).

The large value of D ($84.2 \pm 0.6 \times 10^{-2} \mu\Omega\text{-cm/K}^{1/2}$) for Co-doped $\text{Ni}_2\text{Mn}_{1+x}\text{In}_{1-x}$ compared to that for Ni–Mn–Sn ($9.1 \pm 0.5 \times 10^{-2} \mu\Omega\text{-cm/K}^{1/2}$) and Ni–Mn–In ($11.3 \pm 0.3 \times 10^{-2} \mu\Omega\text{-cm/K}^{1/2}$) alloys implies that these alloys have higher structural and magnetic disorder. This might be the influence of quenched atomic disorder.

Magneto-transport trend

The MR in the Ni–Mn-based Heusler alloys has attracted attention of researchers since 2005, after Biswas *et al.*³⁰

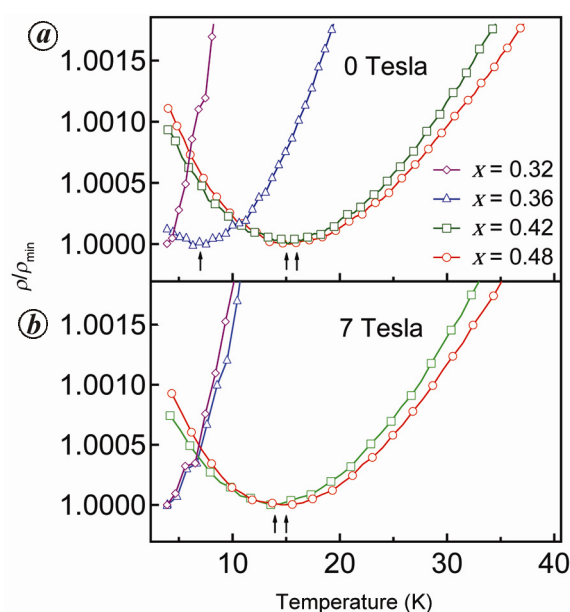


Figure 13. Resistivity (ρ) divided by resistivity minimum (ρ_{\min}) as a function of temperature under 0 T and 7 T for $\text{Ni}_2\text{Mn}_{1+x}\text{In}_{1-x}$ (ref. 35).

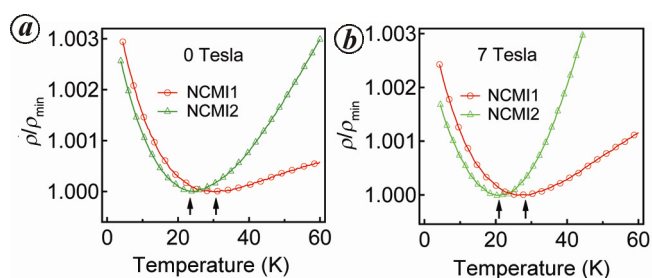


Figure 14. Resistivity (ρ) divided by resistivity minimum (ρ_{\min}) as a function of temperature for NCM1 and NCM2 under (a) 0 T and (b) 7 T.

reported -5% MR at room-temperature in ferromagnetic shape memory alloy $\text{Ni}_{2+x}\text{Mn}_{1-x}\text{Ga}$. The MR is found to increase with x . While MR for $x = 0$ varies almost linearly in the austenitic and pre-martensitic phases, in the martensitic phase it shows a cusp-like shape (Figure 15). This has been explained by the changes in twin and domain structures in the martensitic phase³⁰.

The large MR is observed across the martensitic transformation of Ni–Mn–Sn, Ni–Mn–In and Ni–Co–Mn–In alloys. The large MR of -36% and -81% within the martensitic transition temperature range is observed in $\text{Ni}_2\text{Mn}_{1.4}\text{Sn}_{0.6}$ (Figure 16) and $\text{Ni}_2\text{Mn}_{1.36}\text{In}_{0.64}$ (Figure 17a) respectively. The large MR is due to the magnetic field-induced reverse phase transformation which is because of spin alignment in ferromagnetic state favouring L_2 lattice of austenitic phase through spin lattice coupling. The large difference in the FC and ZFC MR is observed in the martensitic phase of $\text{Ni}_2\text{Mn}_{1.36}\text{In}_{0.64}$ (Figure

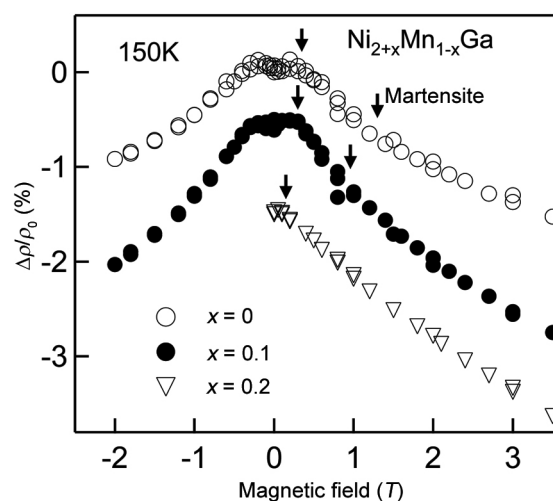


Figure 15. MR of $\text{Ni}_{2+x}\text{Mn}_{1-x}\text{Ga}$ ($x = 0, 0.1$ and 0.2) in the martensitic phase. Arrows indicate the points of inflection. The curves for $x = 0.1$ and $x = 0.2$ are staggered by -0.5% and -1.5% respectively, for clarity of presentation³⁰.

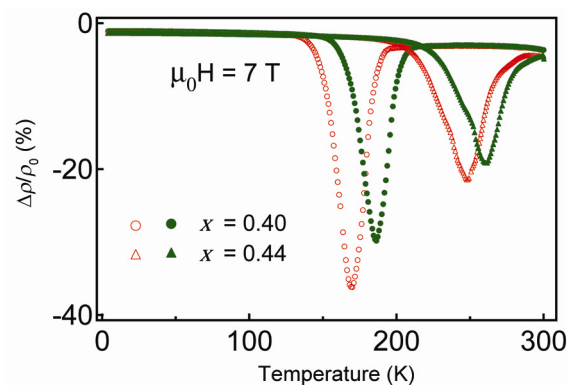


Figure 16. MR as a function of temperature at 7 T for $x = 0.40$ and $x = 0.44$ ($\text{Ni}_2\text{Mn}_{1+x}\text{Sn}_{1-x}$) during cooling (open symbol) and heating (filled symbol)³¹.

17). With FC and ZFC at 5 K, the maximum MR is -79% and -3.1% respectively at 7 T (Figure 17b). The large MR with FC is because of the austenitic phase that has structural and magnetic ordering. Whereas with ZFC the MR is small. This is because the martensitic phase is present where magnetization rotation within twin and reduction of twin boundary scattering occur. This large

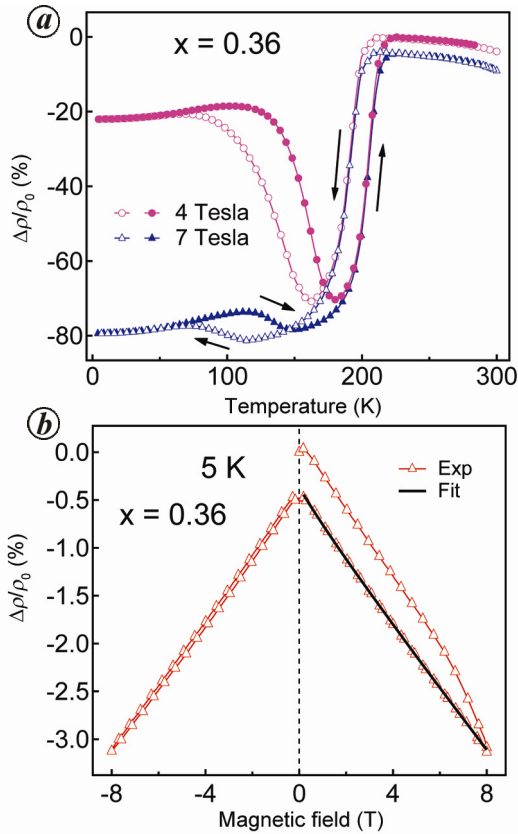


Figure 17. For $x = 0.36$ ($\text{Ni}_2\text{Mn}_{1+x}\text{In}_{1-x}$), (a) FC (open symbol) and FH (filled symbol) MR as a function of temperature at different fields and (b) ZFC MR at 5 K (ref. 33).

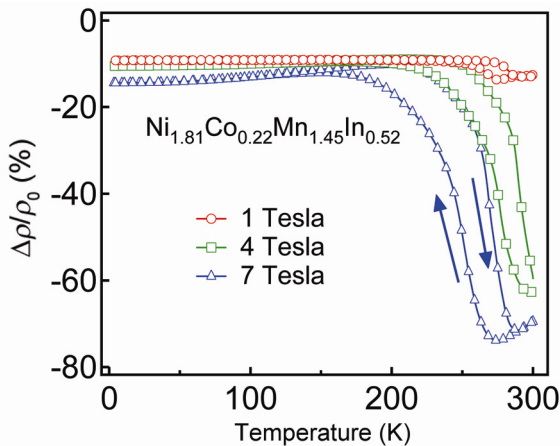


Figure 18. FC MR as a function of temperature for $\text{Ni}_{1.81}\text{Co}_{0.22}\text{Mn}_{1.45}\text{In}_{0.52}$.

difference in FC and ZFC MR of Ni–Mn–In makes the system flexible for application. This is not achieved in Ni–Mn–Sn. Although large MR (-81%) is obtained in Ni–Mn–In alloy, it is achieved much below room temperature (115 K). Co doping at Ni site in Ni–Mn–In alloy exhibits large negative MR (-70%) at room temperature (Figure 18). Thus Ni–Co–Mn–In alloys are a more promising candidate for room-temperature applications.

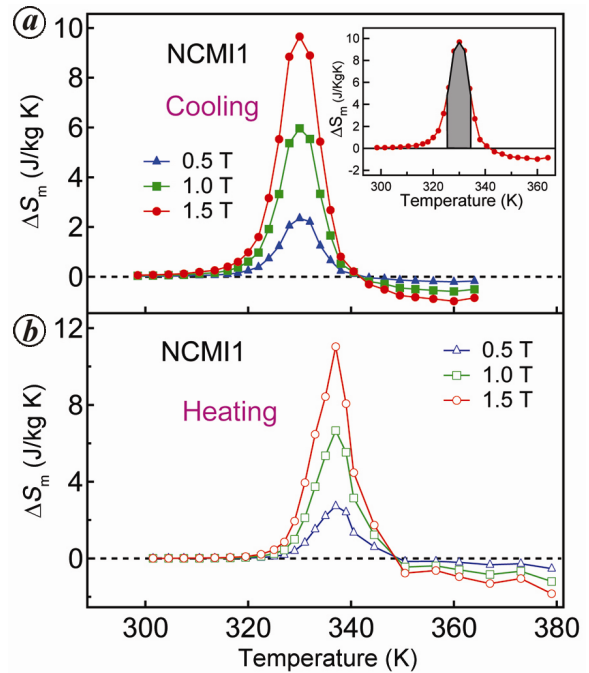


Figure 19. Entropy change S_m for $\text{Ni}_{1.81}\text{Co}_{0.22}\text{Mn}_{1.46}\text{In}_{0.51}$ during (a) cooling, (b) heating³⁹.

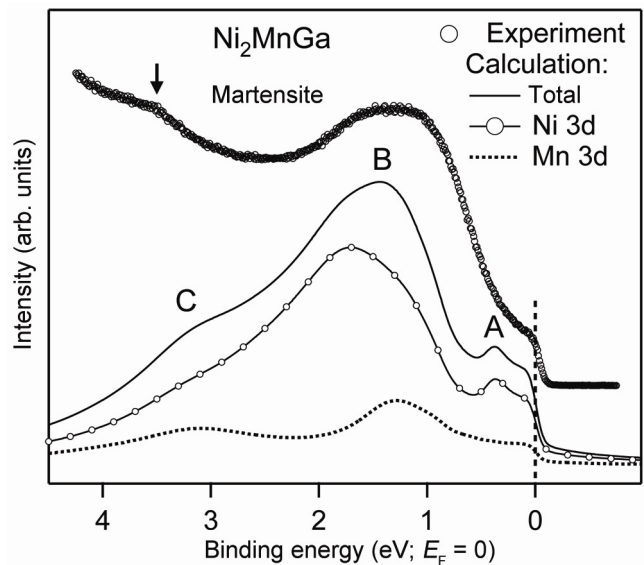


Figure 20. Experimental and calculated valence band spectra of Ni_2MnGa in the martensitic phase. Contributions from Ni and Mn 3d states to the calculated spectrum are shown³⁶.

Magnetocaloric effect

The application of magnetic field in the vicinity of the martensitic transition results in large MCE effect in Ni–Mn–Ga alloys. When structural and magnetic transition temperatures are near to other, the MCE is maximum. The inverse MCE is also observed in near stoichiometric compositions of Ni–Mn–Ga. However, inverse MCE vanishes at high magnetic field⁵⁰. The magnitude of inverse MCE (ΔS_m) is 20 J/kg K at 300 K for 5 T applied field in Ni–Mn–Sn alloys⁵¹. Although the magnitude of MCE is comparable to existing giant MCE materials, the magnetic field required is very high. For Ni–Mn–In, the $\Delta S_m = 12$ J/kg K around 235 K with 5 T applied magnetic field⁵². Thus, the challenge is to obtain similar magnitude of inverse MCE near room temperature with minimum applied magnetic field. Thus, the MCE in Ni–Co–Mn–In alloys is studied at low magnetic field, across the first-order magneto-structural transition. Co-doping at Ni site induces the large magnetic entropy change above room temperature. The large ΔS_m of 11 J/kg K is observed for $\text{Ni}_{1.81}\text{Co}_{0.22}\text{Mn}_{1.46}\text{In}_{0.51}$ alloy at 337 K with an applied field of 1.5 T (Figure 19). The atomic disorder is known to significantly increase the peak value of ΔS_m and decrease the peak width³⁹. The refrigeration capacity is almost unchanged with atomic disorder³⁹. The peak value ΔS_m can be maximized by inducing more atomic disorder in the system. However, ΔT_{RC} of the disordered system decreases compared to the ordered system. Thus, depending on the requirement, the ordered and disordered systems could be utilized for magnetic refrigeration.

Electronic structure

All the above-mentioned properties are closely related to density of states near Fermi energy. Thus, understanding of electronic structure is required to design the possible modifications for a particular application. A detailed study of Ni-doped $\text{Ni}_{2+x}\text{Mn}_{1-x}\text{Ga}$ shows that the valance band (VB) spectra are dominated by the Ni 3d–Mn 3d states and are in good agreement with theory (Figure 20)³⁶. The XPS difference spectrum between $x = 0$ and $x = 0.2$ shows a feature at 0.6 eV that is in good agreement with the Ni metal 3d states. The experimental UPS difference spectrum between $x = 0.2$ and $x = 0$ (Figure 21) also shows extra states in the former around 0.65 eV. These extra states are related to bonding between doped Ni at Mn position and Ni atoms at Ni position. The Ga 4s, p states are observed at 7.7 eV BE (Biswas⁵³; figure 7.13).

A satellite feature is observed in Ni 2p core level, whose origin is similar to that in Ni metal. It is found that the band width ($W = 5.3$ eV) is smaller than the core hole–3d Coulomb interaction ($U_{dc} = 5.9$ eV), which is the reason for the appearance of the satellite feature. The Mn

3s exchange splitting decreases with x , which indicates decrease in Mn magnetic moment with Ni doping⁵⁴.

The Mn substitution at Sn site does not affect Ni core-level states in Ni–Mn–Sn. The Mn core-level states undergo BE shift due to change in local environment (Figure 22). The local Mn moment also increases with increase in Mn concentration⁵⁵. The Sn core level is also unaffected by Mn

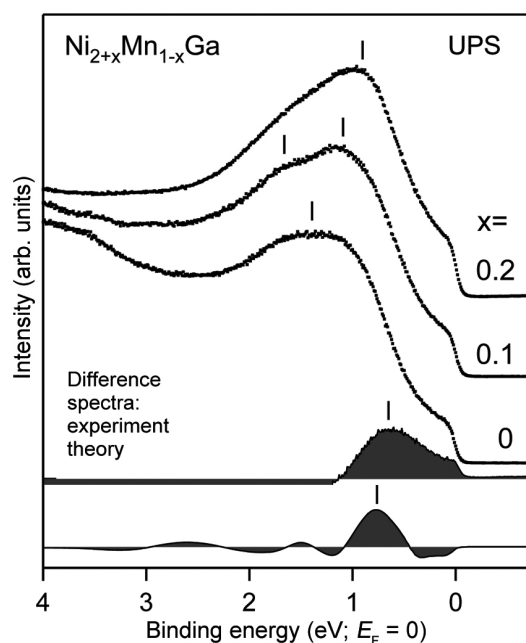


Figure 21. UPS spectra of $\text{Ni}_{2+x}\text{Mn}_{1-x}\text{Ga}$ in the martensitic phase. The spectra have been normalized to the same height. The experimental difference spectrum between $x = 0.2$ and $x = 0$ is compared with the calculated difference spectrum between $x = 0.25$ and $x = 0$ (ref. 36).

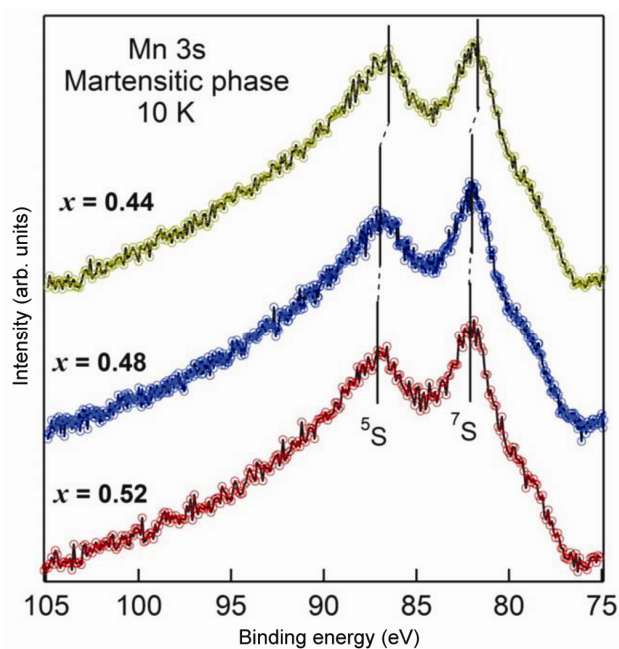


Figure 22. Mn 3s spectra of $\text{Ni}_{2+x}\text{Mn}_{1-x}\text{Sn}_{1-x}$ in the martensitic phase. The spectra are recorded with 1486.6 eV photon energy at 10 K (ref. 55).

substitution. The band width of VB as a function of Mn2 concentration remains the same. The number of holes in Ni–Mn–Sn compared to that for Ni metal is less. The effect of Ni 3d–Mn 3d state hybridization is manifested through Ni satellite⁵⁵. The martensitic transformation in Ni₂Mn_{1+x}Sn_{1-x} alloys has been studied within *ab initio* DFT⁴⁰. The martensitic transformation is obtained for $x = 0.375$, which is in good agreement with the experimental value of $x = 0.36$. The relative on-site energies of Ni d states are very less in cubic and fully relaxed tetragonal structure of Ni₂Mn_{1.5}Sn_{0.5}. This implies that the Jahn–Teller effect could not be the driving force for the martensitic transition as predicted for these systems. Also, the Ni–Mn hybridization alone is not responsible for martensitic transition. The presence of Sn lone pair effect on Ni makes the cubic structure unstable and triggers the structural transformation in Ni–Mn–Sn systems.

The trend of site occupation of Co at Ni sites of Ni₂MnIn system is also studied in the austenitic phase by *ab initio* DFT calculation. The Co atoms prefer to be at Ni site rather than at Mn site. The Co spin is ferromagnetically coupled with that of Ni and Mn. The martensitic ground state has tetragonal structure for Ni_{1.5}Co_{0.5}MnIn and Ni_{1.25}Co_{0.75}MnIn. The doped Co tends to form a cluster rather than random distribution Co (ref. 56).

Further, the trend of site occupation of Mn at Sn sites of Ni₂Mn_{1+x}Sn_{1-x} systems is studied in the austenitic phase by *ab initio* DFT calculation. The excess Mn randomly occupies the Sn site instead of forming a cluster. The Mn1 is antiferromagnetically coupled with Mn2. The martensitic phase stabilizes with orthorhombic structure (Pal *et al.*⁴¹; figure 1).

Surface characterization

For device application of Heusler alloys, thin films are required. Since the properties of MSMA are composition-dependent, proper characterization of the surface is also required that could lead to possible mechanisms of handling thin films. For this purpose, a clean Ni_{2.1}Mn_{0.9}Ga surface with bulk composition is obtained by sputtering and annealing. The surface becomes Ni-rich by sputtering. By annealing the sputtered surface, the bulk composition could be regained. The annealing compensates Mn loss due to sputtering. Figure 23 shows the effect of annealing on composition of sputtered surface. The bulk composition is obtained at 390°C annealing temperature. Similarly, the surface of nearly stoichiometric Ni–Mn–Sn and Ni–Mn–In surface after sputtering and annealing is studied by inverse photoemission and photoemission spectroscopy. The annealing of sputtered surface at about 580 and 500–700 K is enough to produce stoichiometric composition of Ni–Mn–Sn and Ni–Mn–In respectively³⁸. The spectral shapes of Ni–Mn–In and Ni–Mn–Sn are quiet similar (compare Figure 24 and figure 4 of Maniraj *et*

*al.*³⁸). The dominant feature in experimental and calculated IPES is related to the Mn 3d-like state (Figure 24). The Ni 3d and Mn 3d states contribute near the Fermi edge. The peak position in the calculated spectra of Ni–Mn–In (shown by an arrow in figure 4 of Maniraj *et al.*³⁸) is around 1.2 eV above E_F . Whereas that for Ni–Mn–Sn is around 1 eV above E_F (Figure 24). The difference in peak position between Ni₂MnIn and Ni₂MnSn could be related to rigid band effect. The outer shell configuration of In is 5s²5p¹ and that of Sn is 5s²5p². Thus, the extra 5p electron in the valence band of Sn causes a shift of E_F . Moreover, the calculated IPES spectra of Ni₂MnSn (Figure 24) and Ni₂MnIn also exhibit similar features with similar shift (figure 4 of Maniraj *et al.*³⁸). This confirms that the difference in peak position between Ni₂MnIn and Ni₂MnSn is due to the rigid band shift.

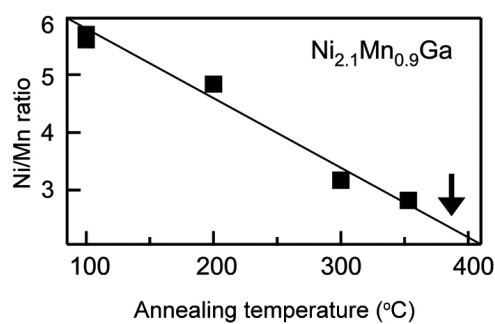


Figure 23. Ni : Mn ratio as a function of annealing temperature fitted by a straight line. Arrow shows the temperature where the bulk composition is restored⁵⁷.

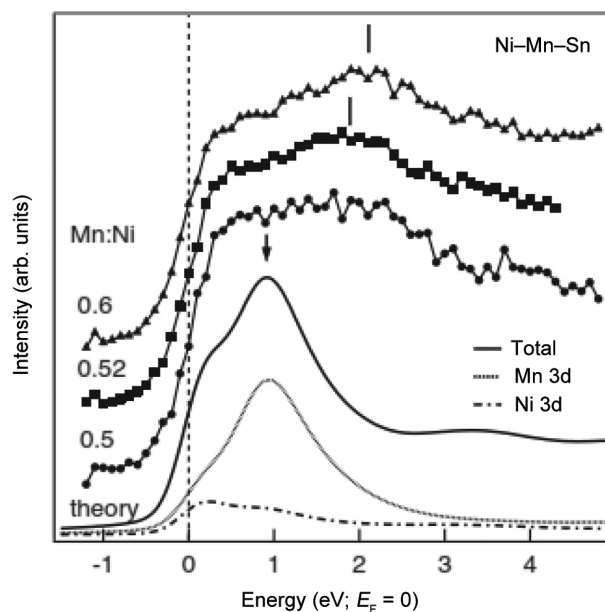


Figure 24. IPES spectra measured at room-temperature for different surface compositions of Ni–Mn–Sn as indicated by the Mn : Ni ratio. The convoluted total density of states and partial density of states are also shown³⁸.

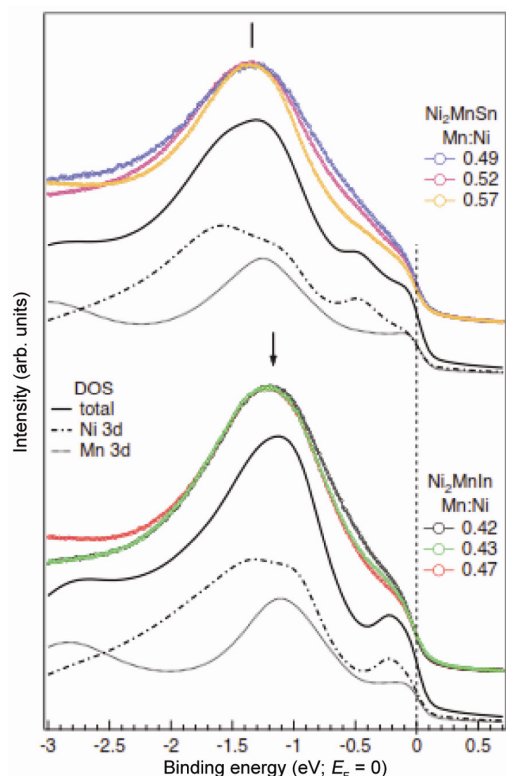


Figure 25. He I UPS valence band spectra measured for different surface compositions of Ni–Mn–Sn and Ni–Mn–In as indicated by the Mn : Ni ratio. The calculated valence band for Ni_2MnSn and Ni_2MnIn , and Ni 3d and Mn 3d contributions to the calculated valence band are also shown³⁸.

The experimentally obtained UPS valence band spectra could very well be explained by the theoretically obtained spectra (Figure 25). The calculated partial density of states shows that the UPS valence band is dominated by Ni 3d states for both Ni_2MnSn and Ni_2MnIn (Figure 25). The Mn 3d states are observed near the Ni 3d states. Thus, the main feature of VB arises due to Ni 3d–Mn 3d hybridized states. This is realized in the composition-dependent spectra of NiMnSn. The peak broadening and increase in intensity at about 0.4 eV are observed with decreasing Mn : Ni ratio. Further, the spectral weight in the vicinity of E_F increases with decreasing Mn : Ni ratio. This is due to change in Ni 3d and Mn 3d state hybridization (Figure 25).

Conclusion

The two types of MSMAs were analysed to improve the possibility of applications. It is revealed that the second kind of Heusler alloy, where MFIS is driven by magnetic field induced reverse phase transition, is suitable for magnetic refrigeration and sensors. The Co-doping at the Ni site in Ni–Mn–In alloy makes the applicability at room temperature possible. The applications are possible with polycrystalline alloys, unlike Ni_2MnGa . The disorder

in the second kind of MSMA is, mainly, magnetic in nature due to substitution of Sn by Mn. This disorder induces anti-ferromagnetic coupling. Thus, ferro and anti-ferromagnetic coupling co-exist. Further, the structural disorder leads to spin-glass like state in the second kind of MSMA. The Ni 3d–Mn 3d hybridization occurs for both the kinds of MSMA. However, lone pair of Sn mainly drives martensitic transition in Ni–Mn–Sn. The surface of Ni–Mn–Ga could be prepared by sputtering and annealing. However, the second kind of MSMA surface stabilizes around stoichiometric composition. The shift of E_F in Ni–Mn–In is due to rigid band shift. It is suggested that properties of the second kind of MSMA could be improved by suitable doping. This creates further interest in exploring the second kind of MSMA.

1. Humbeeck, J. V., Non-medical applications of shape memory alloys. *Mater. Sci. Eng. A*, 1999, **273–275**, 134–148.
2. Sun, L. *et al.*, Stimulus-responsive shape memory materials: a review. *Mater. Des.*, 2012, **33**, 577–640.
3. Petrini, L. and Migliavacca, F., Biomedical applications of shape memory alloys. *J. Metall.*, 2011, **2011**, 1–15.
4. Song, C., History and current situation of shape memory alloys devices for minimally invasive surgery. *Open Med. Dev. J.*, 2010, **2**, 24–31.
5. Morgan, N. B., Medical shape memory alloy applications – the market and its products. *Mater. Sci. Eng. A*, 2004, **378**, 16–23.
6. Machado, L. G. and Savi, M. A., Medical applications of shape memory alloys. *Braz. J. Med. Biol. Res.*, 2003, **36**, 683–691.
7. Mantovani, D., Shape memory alloys: properties and biomedical applications. *JOM*, 2000, **52**, 36–44.
8. Duerig, T., Pelton, A. and Stöckel, D., An overview of nitinol medical applications. *Mater. Sci. Eng. A*, 1999, **273–275**, 149–160.
9. Bil, C., Massey, K. and Abdullah, E. J., Wing morphing control with shape memory alloy actuators. *J. Intell. Mater. Syst. Struct.*, 2013, **24**, 879–898.
10. Hartl, D. J. and Lagoudas, D. C., Aerospace applications of shape memory alloys. *Proc. Inst. Mech. Eng. Part G*, 2007, **221**, 535–552.
11. McDonald, S. L., Shape memory alloy applications in space systems. *Mater. Des.*, 1991, **12**, 29–32.
12. Kheirikhah, M., Rabiee, S. and Edalat, M., A review of shape memory alloy actuators in robotics. In *RoboCup 2010: Robot Soccer World Cup XIV* (eds Ruiz-del-Solar, J., Chown, E. and Pflger, P.), Springer, Berlin, 2011, pp. 206–217.
13. Sreekumar, M., Nagarajan, T., Singaperumal, M., Zoppi, M. and Molfino, R., Critical review of current trends in shape memory alloy actuators for intelligent robots. *Ind. Robot. Int. J.*, 2007, **34**, 285–294.
14. Furuya, Y. and Shimada, H., Shape memory actuators for robotic applications. *Mater. Des.*, 1991, **12**, 21–28.
15. Wu, M. H. and Schetky, L. M., Industrial applications for shape memory alloys. In *International Conference on Shape Memory and Superelastic Technologies*, California, USA, 2000, pp. 171–182.
16. Zider, R. B. and Krumme, J. F., Eyeglass frame including shape-memory elements. US Patents 4772112, CVI/Beta Ventures, Inc., California, USA, 1988.
17. Hautcoeur, A. and Eberhardt, A., Eyeglass frame with very high recoverable deformability. US Patents 5640217, Fergaflex, Inc., Montreal, Canada, 1997.
18. Furuya, Y., Design and material evaluation of shape memory composites. *Intell. Mater. Syst. Struct.*, 1996, **7**, 321–330.
19. Leo, D. J., Weddle, C., Naganathan, G. and Buckley, S. J., Vehicular applications of smart material systems. In *Proceedings of the SPIE 3326, Smart Structures and Materials 1998: Industrial and*

- Commercial Applications of Smart Structures Technologies, San Diego, CA, 1998, pp. 106–116.
20. Stoeckel, D., Shape memory actuators for automotive applications. *Mater. Des.*, 1990, **11**, 302–307.
 21. Butera, F., Coda, A. and Vergani, G., Shape memory actuators for automotive applications. In *Nanotec IT Newsletter*, AIRI/Nanotec IT, Roma, 2007, p. 1216.
 22. Kohl, M., *Shape Memory Microactuators (Microtechnology and MEMS)*, Springer-Verlag Berlin, 2010, 1st edn.
 23. Kahny, H., Huffz, M. A. and Heuer, A. H., The TiNi shape-memory alloy and its applications for MEMS. *Micromech. Microeng.*, 1998, **8**, 213–221.
 24. Fujita, H. and Toshiyoshi, H., Micro actuators and their applications. *Microelectron. J.*, 1998, **29**, 637–640.
 25. Langenhove, L. V. and Hertler, C., Smart clothing: a new life. *Int. J. Clothing Sci. Technol.*, 2004, **16**, 63–72.
 26. Hamzic, A., Asomoza, R. and Campbell, I. A., The transport properties of Heusler alloys: ‘ideal’ local moment ferromagnets. *J. Phys. F*, 1981, **11**, 1441.
 27. Kbler, J., Williams A. R. and Sommers, C. B., Formation and coupling of magnetic moments in Heusler alloys. *Phys. Rev. B*, 1983, **28**, 1745.
 28. Karaca, H. E., Karaman, I., Basaran, B., Ren, Y., Chumlyakov, Y. I. and Maier, H. J., Magnetic field-induced phase transformation in NiMnCoIn magnetic shape-memory alloys: a new actuation mechanism with large work output. *Adv. Funct. Mater.*, 2009, **19**, 983.
 29. Karaca, H. E., Karaman, I., Basaran, B., Chumlyakov, Y. I. and Maier, H. J., Magnetic field and stress induced martensite reorientation in NiMnGa ferromagnetic shape memory alloy single crystals. *Acta Mater.*, 2006, **54**, 233.
 30. Biswas, C., Rawat, R. and Barman, S. R., Large negative magnetoresistance in a ferromagnetic shape memory alloy: Ni_{2+x}Mn_{1-x}Ga. *Appl. Phys. Lett.*, 2005, **86**, 202508, 2005.
 31. Singh Sandeep and Biswas, C., Magnetoresistance origin in martensitic and austenitic phases of Ni₂Mn_{1+x}Sn_{1-x}. *Appl. Phys. Lett.*, 2011, **98**, 212101.
 32. Krenke, T., Acet, M., Wassermann, E. F., Moya, X., Maosa, L. and Planes, A., Ferromagnetism in the austenitic and martensitic states of NiMnIn alloys. *Phys. Rev. B*, 2006, **73**, 174413.
 33. Singh, Sandeep, Illya, G. and Biswas, C., Field-cooled and zero-field cooled magnetoresistance behaviour of Ni₂Mn_{1+x}In_{1-x} alloys. *J. Alloys Compd.*, 2014, **615**, 994–997.
 34. Singh, Sandeep, Pal, Soumyadipta and Biswas, C., Disorder induced resistivity anomaly in Ni₂Mn_{1+x}Sn_{1-x}. *J. Alloys Compd.*, 2014, **616**, 110–115.
 35. Singh, Sandeep and Biswas, C., Resistivity behaviour of Ni₂Mn_{1+x}In_{1-x} magnetic shape memory alloys at low temperature. *Intermetallics*, 2016, submitted.
 36. Chakrabarti, Aparna, Biswas, C., Banik, S., Dhaka, R. S., Shukla, A. K. and Barman, S. R., Influence of Ni doping on the electronic structure of Ni₂MnGa. *Phys. Rev. B*, 2005, **72**, 073103.
 37. Singh, Sandeep, Ganesh, A., Biswas, D., Kalobaran, M. and Biswas, C., Electronic structure modification of Ni₂Mn_{1.4}Sn_{0.6} upon martensitic phase transition. *AIP Conf. Proc.*, 2011, **1349**, 849–850.
 38. Maniraj, M., DSouza, S. W., Singh, Sandeep, Biswas, C., Majumdar, S. and Barman, S. R., Inverse photoemission and photoemission spectroscopic studies on sputter-annealed Ni–Mn–Sn and Ni–Mn–In surfaces. *J. Electron Spectrosc. Relat. Phenom.*, 2014, **197**, 106–111.
 39. Singh, Sandeep, Illya, G. and Biswas, C., The influence of quench atomic disorder on the magnetocaloric properties of Ni–Co–Mn–In alloys. *J. Alloys Compd.*, 2014, **601**, 108–111.
 40. Pal, Soumyadipta, Sagar, S., Pandey, S. K., Chhayabrita, M. and Mahadevan, P., Driving force for martensitic transformation in Ni₂Mn_{1+x}Sn_{1-x}. *Phys. Rev. B*, 2016, **94**, 115143.
 41. Pal, Soumyadipta, Mahadevan, P. and Biswas, C., Role of excess Mn for martensitic transformation in Ni₂Mn_{1+x}Sn_{1-x}: *ab initio* approach. *AIP Conf. Proc.*, 2014, **1591**, 58.
 42. Sokolovskiy, V. V., Buchelnikov, V. D., Zagrebin, M. A., Entel, P., Sahoo, S. and Ogura, M., First-principles investigation of chemical and structural disorder in magnetic Ni₂Mn_{1+x}Sn_{1-x} Heusler alloys. *Phys. Rev. B*, 2012, **86**, 134418.
 43. Chatterjee, S., Giri, S., De, S. K. and Majumdar, S., Reentrant-spin-glass state in Ni₂Mn_{1.36}Sn_{0.64} shape-memory alloy. *Phys. Rev. B*, 2009, **79**, 092410.
 44. Umetsu, R. Y., Fujita, A., Ito, W., Kanomata, T. and Kainuma, R., Determination of the magnetic ground state in the martensite phase of Ni–Mn–Z (Z = In, Sn and Sb) off-stoichiometric Heusler alloys by nonlinear AC susceptibility. *J. Phys.: Condens. Matter*, 2011, **23**, 326001.
 45. Hurd, C. M., Shiozaki, I. and McAlister, S. P., Electrical and magnetic properties of Pd₂MnIn, Pd₂MnSn, Cu₂MnAl and Cu₂NiSn Heusler alloys, *Phys. Rev. B*, 1982, **26**, 701.
 46. McAlister, S. P., Shiozaki, I., Hurd, C. M. and Stager, C. V., Galvanomagnetic effects in the Ni₂MnSn Heusler alloy. *J. Phys. F*, 1981, **11**, 2129.
 47. Zhou, Y., Jin, X., Xu, H., Kudryavtsev, Y. V., Lee, Y. P. and Rhee, J. Y., Influence of structural transition on transport and optical properties of Ni₂MnGa alloy. *J. Appl. Phys.*, 2002, **91**, 9894.
 48. Barandiarn, J. M., Chernenko, V. A., Lzpita, P., Gutierrez, J. and Feuchtwanger, J., Effect of martensitic transformation and magnetic field on transport properties of Ni–Mn–Ga and Ni–Fe–Ga Heusler alloys. *Phys. Rev. B*, 2009, **80**, 104404.
 49. Chatterjee, S., Giri, S., Majumdar, S. and De, S. K., Thermomagnetic irreversibility in Ni₂Mn_{1.36}Sn_{0.64} shape-memory alloy. *Phys. Rev. B*, 2008, **77**, 224440.
 50. Marcos, J., Maosa, L., Planes, A., Casanova, F., Batlle, X. and Labarta, A., Multiscale origin of the magnetocaloric effect in Ni–Mn–Ga shape-memory alloys. *Phys. Rev. B*, 2003, **68**, 094401.
 51. Krenke, T., Duman, E., Acet, M., Wassermann, E. F., Moya, X., Maosa, L. and Planes, A., Inverse magnetocaloric effect in ferromagnetic NiMnSn alloys. *Nature Mater.*, 2005, **4**, 450–454.
 52. Sokolovskiy, V. V., Zagrebin, M. A. and Buchelnikov, V. D., *Shape Memory Alloys: Properties, Technologies, Opportunities* (ed. Natalia Resnina and Vasili Rubanik), 2015, p. 38.
 53. Biswas, C., Electronic structure studies of metals and intermetallics, Ph D thesis, 2005.
 54. Biswas, C., Banik, S., Shukla, A. K., Dhaka, R. S., Ganesan, V. and Barman, S. R., Surface composition and electronic structure of Ni_{2+x}Mn_{1-x}Ga studied by X-ray photoelectron spectroscopy. *Surf. Sci.*, 2006, **600**, 3749–3752.
 55. Singh, Sandeep, Ganesh, A., Biswas, D., Kalobaran, M. and Chhayabrita, M., Electronic structure of Ni₂Mn_{1+x}Sn_{1-x} as a function of composition. *AIP Conf. Proc.*, 2017.
 56. Pal, Soumyadipta, Mahadevan, P. and Biswas, C., Site occupancy trend of Co in Ni₂MnIn: *ab initio* approach. *AIP Conf. Proc.*, 2015, **1665**, 090020.
 57. Biswas, C. and Barman, S. R., X-ray photoelectron spectroscopy study of sputter-annealed Ni_{2.1}Mn_{0.9}Ga surface. *Appl. Surf. Sci.*, 2006, **252**, 3380–3385.
- ACKNOWLEDGEMENTS. I thank Dr S. R. Barman and his group (UGC-DAE CSR, Indore), Prof. Priya Mahadevan and her group (SNBoseNCBS, Kolkata), Prof. Kalobaran Maiti and his group (TIFR, Mumbai), Dr Rajeev Rawat (UGC-DAE CSR, Indore), Prof. P. K. Mukhopadhyay (SNBoseNCBS, Kolkata), and Dr Illya Glavatskiy (HZB, Berlin) for providing experimental and theoretical tools. I also thank Prof. B. N. Dev and Prof. G. P. Das (IACS, Kolkata) for fruitful discussions; my students Dr Sandeep Singh and Mr Soumyadipta Pal for performing the experiments and analysis, and DST, New Delhi for financial support vide reference no SR/WOS-A/PM-11/2016 under WOS-A.

doi: 10.18520/cs/v112/i07/1390-1401